Analytical Point Spread Functions for 3D Full Vectorial Inverse Source Imaging

Georg Schnattinger [#1], Thomas F. Eibert [#]

[#] *Lehrstuhl für Hochfrequenztechnik, Technische Universität München*
80290 Munich, Germany (e-mail: hft@ei.tum.de)
[1] georg.schnattinger@tum.de

Abstract—3D full vectorial inverse source problems can be solved by imaging principles. Point spread functions can be used to estimate the system response of imaging systems to unknown target objects. Typically, point spread functions are obtained by numerical simulations. However, this can be computationally demanding or the result might be inaccurate. In some cases, an analytical solution which does not have these drawbacks is also feasible. In this work, new analytical point spread functions have been derived for two different sets of observation data. The first set limits the observation data to a narrow angle narrow bandwidth sector and the second set assumes full spherical coverage combined with an arbitrary frequency band. The results have been verified using numerical examples and they can be employed for system simulations and accuracy investigations.

I. Introduction

The well-known topic of electromagnetic imaging is, for example, applied to characterize unknown scattering targets. Recently, we have shown that imaging is also useful for solving full vectorial inverse source problems [1]. The quality of the generated images always depends on many parameters such as bandwidth, frequency, angular scan range and the type of the applied reconstruction technique. So even in case of a correct algorithm, the image does not perfectly resemble the unknown target. The unwanted deviations can be modeled by so-called point spread functions (PSFs) [2]–[7]. In this work, analytical PSFs for full vectorial inverse source imaging are derived in order to improve insight and to have a better tool at hand for accuracy checks.

A brief description of full vectorial inverse source imaging is given in Sec. II, several analytical PSFs are derived in Sec. III, a numerical verification of the results is carried out in Sec. IV and conclusions are drawn in Sec. V.

II. Full Vectorial Inverse Source Imaging

A frequency invariant source distribution is radiating fields in a wide frequency band. The fields are observed in the surrounding volume. The goal is to use these observations to generate an image of the unknown source distribution. In the following paragraph, the mathematical expressions for that purpose are given.

As shown in [1], the approach is applicable both under far-field and near-field conditions. Due to limited space, only far-field observations are considered here. The radiated far-fields read as

$$\mathbf{E}\left(\mathbf{k}\right) = -\frac{jkZ_F}{4\pi}\left(\bar{\mathbf{I}} - \hat{k}\hat{k}\right)\iiint \mathbf{J}\left(\mathbf{r}, k\right)\mathrm{e}^{-j(j\mathbf{k}\cdot\mathbf{r})}d^3\mathbf{r}$$
$$= -\frac{jkZ_F}{4\pi}\left(\bar{\mathbf{I}} - \hat{k}\hat{k}\right)(2\pi)^3\mathcal{F}^{-1}\left\{\mathbf{J}\left(\mathbf{r}, k\right)\right\}, \quad (1)$$

where $\mathbf{J}$ denotes the source distribution, k and $\mathbf{k} = k\hat{k}$ denote the wavenumber and the wavevector, respectively, Z_F is the free-space impedance and the symbols $\mathcal{F}\{\bullet\}$ and $\mathcal{F}^{-1}\{\bullet\}$ denote the 3D Fourier transform and its inverse. In a real application, all data must be sampled appropriately. From the radiated fields, the image is computed according to

$$\mathcal{F}\left\{\frac{\mathbf{E}\left(\mathbf{k}\right)}{k}\right\} \propto \mathcal{F}\left\{\left(\bar{\mathbf{I}} - \hat{k}\hat{k}\right)\right\} \overset{\circ}{*} \mathcal{F}\left\{\mathcal{F}^{-1}\left\{\mathbf{J}\left(\mathbf{r}, k\right)\right\}\right\}, \quad (2)$$

where the symbol $\overset{\circ}{*}$ denotes the element-wise convolution of a dyadic with a vector using the definition of the scalar product. The right-hand side of the expression emphasizes the deviations between the true source distribution and its image. The deviations are caused by the fact that the solution of the corresponding inverse source problem is not unique [8] and it can be shown that the generated image corresponds to the minimum energy solution in case of a frequency invariant source [9]. The dyadic expression in (2) is generalized for various acquisition geometries by

$$\bar{\mathbf{P}}\left(\mathbf{r}\right) = \mathcal{F}\left\{M\left(k\right)\left(\bar{\mathbf{I}} - \hat{k}\hat{k}\right)\right\}$$
$$= \mathcal{F}\left\{M\left(k\right)\right\}\bar{\mathbf{I}} - \mathcal{F}\left\{M\left(k\right)\hat{k}\hat{k}\right\}. \quad (3)$$

In the following section, this PSF will be solved analytically for specific choices of $M\left(k\right)$.

III. Dyadic Point Spread Functions

A. Narrow Angle Narrow Bandwidth Approximation

In many scenarios, field observations are only available in a narrow angular sector with a small relative bandwidth. Based on this assumption, an approximate analytical solution for the PSF can be derived. By defining

$$M\left(\mathbf{k}\right) = \begin{cases} 1 & , \mathbf{k} \in K \\ 0 & , \mathbf{k} \notin K \end{cases} \quad (4)$$

with

$$\mathbf{k} = k \begin{pmatrix} \cos\phi\sin\theta \\ \sin\phi\sin\theta \\ \cos\theta \end{pmatrix} \in K \iff \begin{array}{c} 2\left|\phi - \phi_0\right| \le \Delta\phi \\ 2\left|\theta - \theta_0\right| \le \Delta\theta \\ 2\left|k - k_0\right| \le \Delta k \end{array} \quad (5)$$

for $\theta_0 = \frac{\pi}{2}$ and $\phi_0 = 0$, the line of sight will be aligned with the x-axis. Due to the rotational invariance principle of the Fourier transform [10, pp. 28], the result can be rotated appropriately to match an arbitrary viewing angle. In this case, the dyadic PSF in (3) can be expressed as

$$\int_{-\frac{\Delta k}{2}}^{\frac{\Delta k}{2}} \int_{-\frac{\Delta\phi}{2}}^{\frac{\Delta\phi}{2}} \int_{-\frac{\Delta\theta}{2}}^{\frac{\Delta\theta}{2}} e^{-j\mathbf{k}\cdot\mathbf{r}} \left(\mathbf{k}\cdot\mathbf{k} - \mathbf{kk}\right) \sin\theta \, d\theta \, d\phi \, dk. \quad (6)$$

By expanding the prefactor and the exponent using a multivariate Taylor series of order one with respect to θ, ϕ and k, the analytical solution

$$\bar{\mathbf{P}}(\mathbf{r}) = k_0^2 \, \Delta\phi \, \Delta\theta \, \Delta k \, e^{-jk_0 x} \quad (7)$$
$$\begin{pmatrix} 0 & g_2(\Delta\mathbf{k}, \mathbf{r}, k_0) & g_3(\Delta\mathbf{k}, \mathbf{r}, k_0) \\ g_2(\Delta\mathbf{k}, \mathbf{r}, k_0) & g_1(\Delta\mathbf{k}, \mathbf{r}, k_0) & 0 \\ g_3(\Delta\mathbf{k}, \mathbf{r}, k_0) & 0 & g_1(\Delta\mathbf{k}, \mathbf{r}, k_0) \end{pmatrix},$$

is obtained, where

$$g_1(\Delta\mathbf{k}, \mathbf{r}, k_0) = \operatorname{si}\left(\frac{\Delta\phi k_0 y}{2}\right) \operatorname{si}\left(\frac{\Delta\theta k_0 z}{2}\right)$$
$$\left[\left(1 - \frac{j2}{k_0 x}\right) \operatorname{si}\left(\frac{\Delta k x}{2}\right) + \frac{j2}{k_0 x} \cos\left(\frac{\Delta k x}{2}\right)\right], \quad (8)$$

$$g_2(\Delta\mathbf{k}, \mathbf{r}, k_0) = \frac{j}{k_0 y} \operatorname{si}\left(\frac{\Delta k x}{2}\right) \operatorname{si}\left(\frac{\Delta\theta k_0 z}{2}\right)$$
$$\left[\operatorname{si}\left(\frac{\Delta\phi k_0 y}{2}\right) - \cos\left(\frac{\Delta\phi k_0 y}{2}\right)\right], \quad (9)$$

$$g_3(\Delta\mathbf{k}, \mathbf{r}, k_0) = \frac{j}{k_0 z} \operatorname{si}\left(\frac{\Delta k x}{2}\right) \operatorname{si}\left(\frac{\Delta\phi k_0 y}{2}\right)$$
$$\left[\operatorname{si}\left(\frac{\Delta\theta k_0 z}{2}\right) - \cos\left(\frac{\Delta\theta k_0 z}{2}\right)\right] \quad (10)$$

and

$$\operatorname{si}(x) = \frac{\sin x}{x}. \quad (11)$$

The dyadic PSF is visualized in Fig. 1 using a single y-current located at the origin, i.e. $J(\mathbf{r}) = \delta(\mathbf{r}) \mathbf{e}_y$. In this example, the parameters were set to

$$\lambda \in [1\,\text{m}, 1.5\,\text{m}], \phi_0 = 0, \theta_0 = \frac{\pi}{2}, \Delta\phi = \frac{\pi}{7}, \Delta\theta = \frac{\pi}{19}. \quad (12)$$

The visualization is obtained by projecting the maximum amplitudes onto the faces of a cube. The plot shows that the y-current causes a strong signal in the y-component and a weak signal in the x-component. This can be verified by inspecting the matrix in (7).

More sophisticated results can be obtained by increasing the order of the Taylor expansions. Since the formulas become very large, computer algebra systems such as the MATLAB [11] toolbox MuPAD [12] should be employed. These tools can solve the integrals and then automatically generate program code for the evaluation of the solutions. Tbl. I lists
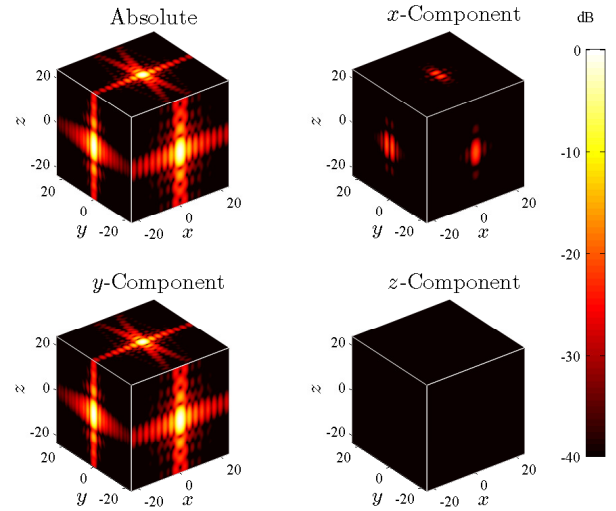

Fig. 1. Image of a single y-current at the origin for the k-space acquisition geometry in (5) generated using (7) for the parameters (12) while x, y and z are measured in wavelengths ($\lambda_{\min}$).

TABLE I
HEURISTIC COMPLEXITY ESTIMATION (EVALUATED WITH MUPAD) OF ANALYTICAL SOLUTION OF INTEGRAL IN (6) APPROXIMATED BY EXPANSION OF PREFACTOR AND EXPONENT IN INTEGRAND UTILIZING MULTIVARIATE TAYLOR SERIES EXPANSION WITH ABSOLUTE ORDER n AND WEIGHTING COFFICIENTS w_k, w_ϕ, w_θ.

Prefactor		Exponent		Heuristic Complexity
n	$[w_k, w_\phi, w_\theta]$	n	$[w_k, w_\phi, w_\theta]$	
1	[2, 1, 1]	1	[1, 1, 1]	375
1	[1, 1, 1]	1	[1, 1, 1]	457
1	[1, 1, 1]	2	[2, 1, 1]	2165
2	[1, 1, 1]	1	[1, 1, 1]	2234
3	[1, 1, 1]	1	[1, 1, 1]	14860
2	[1, 1, 1]	2	[2, 1, 1]	16548
4	[1, 1, 1]	1	[1, 1, 1]	56160
3	[1, 1, 1]	2	[2, 1, 1]	69688

parameters which lead to feasible solutions together with a heuristic complexity estimate of the resulting formulas. The first and the second row correspond to the solutions given in [13] and in (7), respectively. An accuracy analysis of a few selected solutions is given in Sec. IV.

B. Full Scan Range Zero Bandwidth Approximation

Naturally, the image quality increases when more data is available. Thus, the optimum is attained with full spherical coverage. For simplicity, only a single frequency should be considered at first. This setup is accomplished by

$$M(\mathbf{k}) = w(k) = \frac{\delta(k - k_0)}{k^2}. \quad (13)$$

Due to the rotational invariance of the Fourier transform, it is sufficient to evaluate the integrals solely on the z-axis. Thus,
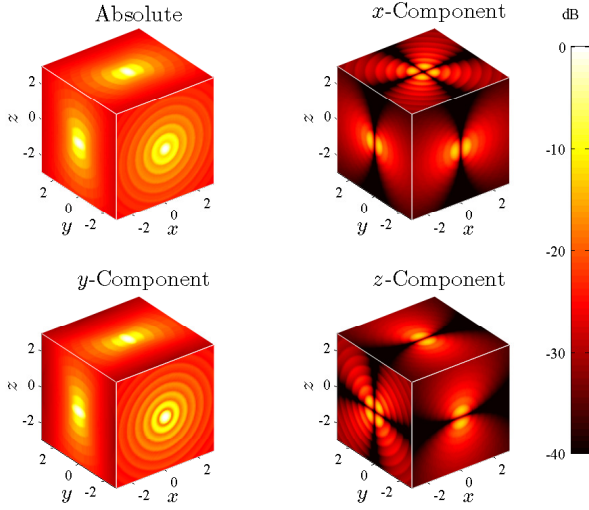
Fig. 2. Image of a single y-current for a monofrequent spherical k-space acquisition geometry generated using (15) for $\lambda = 1\,\mathrm{m}$ while x, y and z are measured in wavelengths (λ).

Fig. 3. Image of a single y-current for a broadband spherical k-space acquisition geometry generated using (17) for $\lambda_{\min} = 1\,\mathrm{m}$ and $\lambda_{\max} = 1.5\,\mathrm{m}$ while x, y and z are measured in wavelengths ($\lambda_{\min}$).

the second term in (3) resolves to

$$\mathcal{F}\left\{w\left(k\right)\hat{k}\hat{k}\right\}\Big|_{\mathbf{r}=r\mathbf{e}_z} =$$

$$= \frac{4\pi}{(k_0 r)^3}\Big[\left(\sin\left(k_0 r\right) - k_0 r\cos\left(k_0 r\right)\right)\left(\mathbf{e}_x\mathbf{e}_x + \mathbf{e}_y\mathbf{e}_y\right) +$$

$$\left(\left(k_0^2 r^2 - 2\right)\sin\left(k_0 r\right) + 2k_0 r\cos\left(k_0 r\right)\right)\mathbf{e}_z\mathbf{e}_z\Big]$$

$$= \frac{4\pi}{(2\pi k_0 r)^3}\Big[\left(\sin\left(k_0 r\right) - k_0 r\cos\left(k_0 r\right)\right)\bar{\mathbf{I}} +$$

$$\left(\left(k_0^2 r^2 - 3\right)\sin\left(k_0 r\right) + 3k_0 r\cos\left(k_0 r\right)\right)\mathbf{e}_z\mathbf{e}_z\Big]. \quad (14)$$

Together with the solution of $\mathcal{F}\left\{w\left(k\right)\right\}$ given in [1], the dyadic PSF finally reads as

$$\bar{\mathbf{P}}\left(\mathbf{r}\right) = \mathcal{F}\left\{w\left(k\right)\right\} - \mathcal{F}\left\{w\left(k\right)\hat{k}\hat{k}\right\} \quad (15)$$

$$= \frac{4\pi}{(k_0 r)^3}\Big[\left(\left(k_0^2 r^2 - 1\right)\sin\left(k_0 r\right) + k_0 r\cos\left(k_0 r\right)\right)\bar{\mathbf{I}} +$$

$$\left(\left(3 - k_0^2 r^2\right)\sin\left(k_0 r\right) - 3k_0 r\cos\left(k_0 r\right)\right)\hat{r}\hat{r}\Big],$$

where the Cartesian unit vectors in (14) have been replaced by their spherical counterparts to extend the valid region of the formula from the z-axis to the whole k-space domain. Fig. 2 depicts a single y-current for monofrequent observations with full spherical coverage using the PSF in (14). As can be seen, each Cartesian component in the images contains contributions from the single current element.

C. Full Scan Range Finite Bandwidth Approximation

In the last subsection, results for monofrequent observations using full spherical coverage have been derived. In this section,
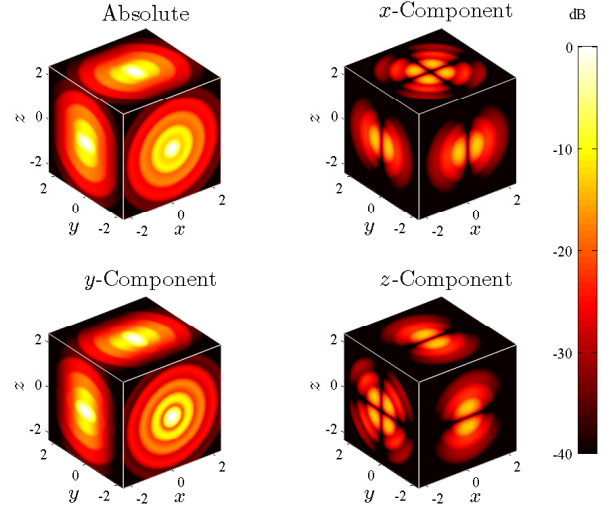
the bandwidth is extended by defining

$$M\left(\mathbf{k}\right) = W\left(k\right) = \begin{cases} 1 & k_{\min} \leq k \leq k_{\max} \\ 0 & \text{otherwise} \end{cases}. \quad (16)$$

The PSF is calculated by applying similar techniques as in the previous section and reads as

$$\bar{\mathbf{P}}\left(\mathbf{r}\right) = \mathcal{F}\left\{W\left(k\right)\right\} - \mathcal{F}\left\{W\left(k\right)\hat{k}\hat{k}\right\} \quad (17)$$

$$= \frac{4\pi}{r^3}\Big[\left(-\operatorname{Si}\left(kr\right) + 2\sin\left(kr\right) - kr\cos\left(kr\right)\right)\bar{\mathbf{I}}$$

$$- \left(-3\operatorname{Si}\left(kr\right) + 4\sin\left(kr\right) - kr\cos\left(kr\right)\right)\hat{r}\hat{r}\Big]_{k_{\min}}^{k_{\max}},$$

where

$$\operatorname{Si}\left(x\right) = \int_0^x \frac{\sin t}{t}\,dt. \quad (18)$$

The result of $\mathcal{F}\left\{W\left(k\right)\right\}$ can be found in [1], [14] and [15, p. 324]. The PSF is shown in Fig. 3. When compared to Fig. 2, the sidelobe level is significantly lower. Note that the magnification is slightly different in both pictures.

IV. NUMERICAL VERIFICATION

To validate the analytical solutions, the numerical algorithm in [1] has been employed as a reference. First, the solutions in Sec. III-A are verified. The scenario from Fig. 1 based on the parameters in (12) is used. The PSF is evaluated on the line defined by

$$\frac{x}{\lambda_{\min}} = -24, ..., 24, \quad \frac{y}{\lambda_{\min}} = 1, \quad \frac{z}{\lambda_{\min}} = 1 \quad (19)$$

using both the numerical algorithm and the solutions in Tbl. I which are given in rows two and eight. Tbl. I lists solutions which have been obtained using the narrow angle narrow bandwidth assumption. The accuracy analysis is presented in
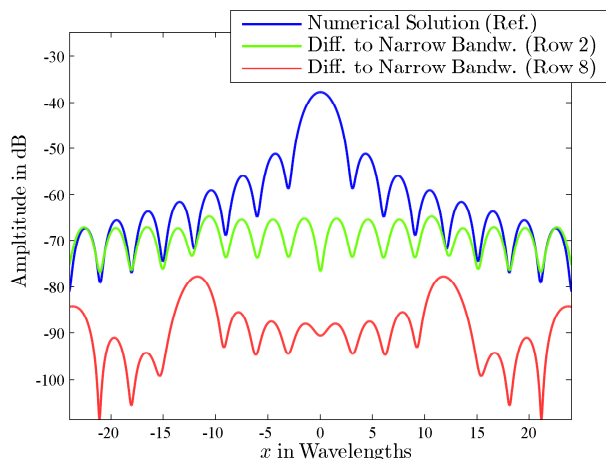
Fig. 4. Comparison of images generated numerically and by PSFs in Table I using the scenario in Fig. 1 and evaluated on the line described by (19).
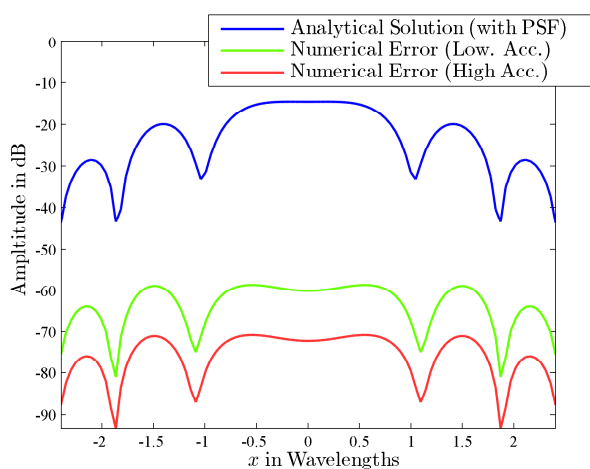

Fig. 5. Comparison of images generated numerically and by PSFs in (17) using the scenario in Fig. 3 and evaluated on the line defined in (20).

Fig. 4, where the first curve in the plot originates from a very accurate numerical solution and the second and third curve represent the error levels of the various analytical solutions. As can be seen, the solution represented by the second curve is only accurate around the main lobe for the given parameters. A higher accuracy is possible with a more sophisticated analytical approximation as indicated by the third curve.

To validate the analytical solution in (15), the scenario depicted in Fig. 3 is adopted. The error was analyzed on the line

$$\frac{x}{\lambda_{\min}} = -2.4, ..., 2.4, \quad \frac{y}{\lambda_{\min}} = 1, \quad \frac{z}{\lambda_{\min}} = 1. \quad (20)$$

Since the analytical solution is exact, it is used as a reference in Fig. 5. The two other curves were obtained by varying the accuracy of the numerical algorithm. It is shown that increasing the accuracy of the numerical algorithm also decreases the error. Therefore, the analytical solution can serve as a reference for the numerical algorithm.

V. CONCLUSION

The images generated by full vectorial inverse source imaging can be described using the concept of dyadic point spread functions (PSFs). In this work, new analytical PSFs have been derived for specific elementary observation domains. A validation has been carried out using numerical examples. The new formulas can be used to simulate imaging algorithms and hopefully provide new insights into the topic.

REFERENCES

[1] G. Schnattinger and T. F. Eibert, "Solution to the full vectorial 3D inverse source problem by multi-level fast multipole method inspired hierarchical disaggregation," *IEEE Trans. Antennas Propag.*, vol. 60, no. 7, pp. 3325–2235, Jul. 2012.

[2] D. L. Mensa, *High Resolution Radar Cross-Section Imaging*, revised ed. Artech House Inc, 1990.

[3] U. K. Majumder, M. A. Temple, M. J. Minardi, and E. G. Zelnio, "Point spread function characterization of a radially displaced scatterer using circular synthetic aperture radar," *IEEE Radar Conference*, pp. 729–733, Apr. 2007.

[4] F. Maussang, F. Daout, G. Ginolhac, and F. Schmitt, "GPS ISAR passive system characterization using point spread function," *New Trends for Environmental Monitoring Using Passive Systems*, pp. 1–4, Oct. 2008.

[5] S. Tathee, Z. J. Koles, and T. R. Overton, "Image restoration in computed tomography: Estimation of the spatially variant point spread function," *IEEE Trans. Med. Imag.*, vol. 11, no. 4, pp. 539–545, Dec. 1992.

[6] G. M. Gallatin, "Analytic evaluation of the intensity point spread function," *Journal of Vaccum Science and Technology B*, vol. 18, no. 6, pp. 3023–3028, Nov. 2000.

[7] F. Berizzi, E. Mese, M. Diani, and M. Martorella, "High-resolution ISAR imaging of maneuvering targets by means of the range instantaneous Doppler technique: modeling and performance analysis," *IEEE Trans. Image Process.*, vol. 10, no. 12, pp. 1880–1890, Dec. 2001.

[8] N. Bleistein and J. K. Cohen, "Nonuniqueness in the inverse source problem in acoustics and electromagnetics," *J. Math. Phys.*, vol. 18, no. 2, pp. 194–201, Feb. 1977.

[9] C. Mller, "Electromagnetic radiation patterns and sources," *IRE Trans. Antennas Propagat.*, vol. 4, no. 3, pp. 224 – 232, Jul. 1956.

[10] J. W. Woods, *Multidimensional Signal, Image, and Video Processing and Coding*. Academic Press, 2011.

[11] *MATLAB*. Natick, Massachusetts: The MathWorks Inc., www.mathworks.com, 2012.

[12] *MuPAD*. SciFace Software, www.mupad.de, 2012.

[13] H. Buddendick and T. F. Eibert, "Bistatic image formation from shooting and bouncing rays simulated current distributions," *Progress In Electromagnetics Research*, vol. 119, pp. 1–18, 2011.

[14] G. Schnattinger, C. H. Schmidt, and T. F. Eibert, "Analysis of 3-D images generated by hierarchical disaggregation," *Proc. Int. Radar Symp. (IRS)*, pp. 365–370, Sep. 2011.

[15] L. Rde and B. Westergren, *Mathematics Handbook for Science and Engineering*, 5th ed. Springer, 2004.